ADVANCED FUNCTIONAL MATERIALS
www.afm-journal.de

Directed Electron Modulation Stabilizes Iridium Oxide Clusters for High-Current-Density Oxygen Evolution

Xian He, Jiaqi Tan, Bohan Deng, Wei Zhao, Zhuting Zhang, Zhichuan Zheng, Yufeng Wu, Chong Yang, Xibo Li, Ming Lei, Hongyi Liu, Kai Huang,* and Hui Wu**

The rapid advancement of the green hydrogen industry has driven a surge in demand for devices that operate over a broad range of current density. Despite this, the development of stable iridium-based catalysts for high-current-density applications in oxygen evolution reactions remains a significant challenge. In this study, directed electron modulation (DEM) of iridium oxide clusters on cobalt hydroxide nanosheets is achieved using a cyclic Joule heating strategy in pure water. The strategy achieves a rapid change of environmental energy during electronic modulation through Joule heating, which ensures strong electronic coupling between IrO_2 and $Co(OH)_2$ without significant changes in initial catalyst nanostructure and cluster size. Directed electron modulation optimizes the reactant adsorption ability of the active center (IrO_2 cluster) and corresponding reaction kinetics are improved, resulting in the catalyst (DEM-IrO_2@$Co(OH)_2$-NF) showing excellent performance. The DEM-IrO_2@$Co(OH)_2$-NF exhibits excellent catalytic activity in alkaline electrolytes with only 296 mV overpotential up to 1 A cm^{-2} and no significant degradation in 1000 h stability test at 1 A cm^{-2}. Additionally, the anion exchange membrane electrolyzer using DEM-IrO_2@$Co(OH)_2$-NF||Pt/C requires only 1.68 V at 1 A cm^{-2} and remains stable for 200 h. This work will provide new directions for optimization of active centers.

1. Introduction

Converting renewable energy into green hydrogen is the cornerstone of the sustainable development of new energy systems. Water electrolysis, which is simple and environmentally friendly, is considered the most promising method for green hydrogen production. The oxygen evolution reaction (OER), as one of the fundamental reactions in water electrolysis, greatly affects the operational cost and efficiency of water electrolysis.[1] Consequently, the development of high-performance OER electrocatalysts remains a research priority.[2] In electrocatalytic reactions, the intrinsic activity and stability of the active center directly determine overall catalyst performance.[3] The optimization and enhancement of active center performance have been the focus of catalysis.[4]

Recently, the decisive role of the surrounding local environment on the performance of active centers has increasingly gained recognition from researchers.[5] Providing appropriate support to the active center and creating a specific local environment to construct supported hierarchical structures can optimize reaction kinetics through the synergistic effect of loading and support.[6] Meanwhile, this strategy can offer suitable pathways for ion diffusion and charge transfer.[7] For example, as a representative element for catalyzing OER, Iridium (Ir), Li et al. utilized the special affinity between manganese and iridium to load stable hexavalent iridium on manganese oxide, which exhibited excellent OER activity.[8] Additionally, supported catalysts constructed with carbon carriers, transition metal-based

X. He, Z. Zheng, Y. Wu, M. Lei, K. Huang
State Key Laboratory of Information Photonics and Optical Communications
School of Science
Beijing University of Posts and Telecommunications
Beijing 100876, P. R. China
E-mail: huang-kai@bupt.edu.cn

X. He, B. Deng, W. Zhao, Z. Zhang, Z. Zheng, Y. Wu, C. Yang, H. Wu
State Key Laboratory of New Ceramics and Fine Processing
School of Materials Science and Engineering
Tsinghua University
Beijing 100084, P. R. China
E-mail: huiwu@tsinghua.edu.cn

J. Tan, X. Li
Siyuan Laboratory, Guangzhou Key Laboratory of Vacuum Coating Technologies and New Energy Materials
Guangdong Provincial Engineering Technology Research Center of Vacuum Coating Technologies and New Energy Materials
Department of Physics
Jinan University
Guangzhou, Guangdong 510632, P. R. China
E-mail: lixibo@jnu.edu.cn

H. Liu
Dongfang Electric (Fujian) Innovation Research Institute Co., Ltd
Fujian 350108, P. R. China

The ORCID identification number(s) for the author(s) of this article can be found under https://doi.org/10.1002/adfm.202416385

DOI: 10.1002/adfm.202416385

compounds, and nitrides have been reported.[9] Particularly, cobalt hydroxide has been extensively studied due to its rich active surface and excellent stability.[10] However, most studies are limited to low current density.[11] With the significant increase in current density standards for industrial electrolyzers, more stringent requirements are placed on the reaction efficiency and stability of catalysts.

Regulating the interfacial structure between loading and support is an effective strategy to further enhance catalyst performance.[12] By directed electron modulation (DEM), strong electronic coupling between loading and support can be achieved, which not only optimizes the reactant adsorption ability to improve catalytic activity but also ensures that the loading remains fixed on support, preventing detachment under high current density.[13] Previous reports indicate that forming directed electron transfer between loading and support typically requires a high-energy environment, which is accompanied by unwanted growth of cluster size and disruption of support nanostructure.[14]

Herein we have successfully realized directed electronic structure modulation of iridium oxide cluster on cobalt hydroxide using cyclic Joule heating (CJH) in pure water. We have utilized the rapid heating-cooling properties of Joule heating to achieve strong electronic coupling between cluster and support while ensuring no significant change in support nanostructure and cluster size. The catalytic electrode (DEM-IrO_2@$Co(OH)_2$-NF) constructed based on this strategy showed excellent activity and stability at high current density, reaching 1 A cm^{-2} at 296 mV overpotential and remaining stable for 1000 h. The density functional theory (DFT) results and in situ Raman revealed that directed electron modulation optimized the reactant adsorption ability of the active center improving the reaction kinetics, and the electron transfer between interfaces stabilized cluster. Moreover, the anion exchange membrane (AEM) electrolyzer using DEM-IrO_2@$Co(OH)_2$-NF||Pt/C required only 1.68 V at 1 A cm^{-2} and maintained high energy efficiency for 200 h under industrial operating conditions, demonstrating the potential for industrial application of DEM-IrO_2@$Co(OH)_2$-NF.

2. Results and Discussion

2.1. Synthesis and Characterization of DEM-IrO2@Co(OH)2-NF Electrode

Due to the porous structure of nickel foam that facilitates mass transfer and its stability in alkaline solution, nickel foam was selected as the growth substrate for the catalyst.[15] **Figure 1a** shows the specific synthesis process. After electrodeposition of $Co(OH)_2$ nanosheets on the nickel foam surface, the precursors were converted to IrO_2 cluster loaded on nanosheets (IrO_2@$Co(OH)_2$-NF) using liquid Joule heating (Figure S1, Supporting Information). Figures S2 and S3 (Supporting Information) show XPS and TEM images of IrO_2@$Co(OH)_2$-NF electrode, and the results show that the supported catalyst with cobalt hydroxide as support and iridium oxide clusters as active center was obtained using liquid Joule heating. Then, the supported catalysts were directed electron modulation using cyclic Joule heating in pure water. Figure S4 (Supporting Information) shows the X-ray diffraction (XRD) spectra of the catalysts before and after electron modulation, and the results show that both IrO_2@$Co(OH)_2$-NF and DEM-IrO_2@$Co(OH)_2$-NF contain only peaks corresponding to Ni and $Co(OH)_2$, which can be attributed to the low Ir loading.[16]

The transmission electron microscopy (TEM) images and energy dispersive X-ray spectroscopy (EDS) elemental maps of DEM- IrO_2@$Co(OH)_2$-NF in Figure 1b show that the directed electron modulation process didn't disrupt the 2D layered structure of $Co(OH)_2$ and the uniform distribution of Ir, Co, and O elements. It is also confirmed by scanning electron microscopy (SEM) images of the samples before and after electron modulation, as shown in Figure S6 (Supporting Information), where the nanosheet morphology was unchanged after electron modulation. In the high-magnification TEM image (Figure 1c), densely and uniformly distributed clusters of DEM- IrO_2@$Co(OH)_2$-NF are observable with an average size of 1.54 ± 0.30 nm (Figure S7, Supporting Information), which is close to the before-modulation size of 1.52 ± 0.30 nm (Figure S8, Supporting Information), suggesting that there is no growth of the clusters during the electron modulation process. According to the results of inductively coupled plasma optical emission (ICP-OES), the iridium loading in DEM- IrO_2@$Co(OH)_2$-NF was 0.091 mg cm^{-2} (Table S1, Supporting Information), which was close to that of 0.098 mg cm^{-2} in IrO_2@$Co(OH)_2$-NF before modulation, indicating that there was no significant iridium loss during the electron modulation process. As mentioned in the introduction, electronic modulation is accompanied by a high-energy environment, which can cause unwanted structural damage. Therefore, pure water is introduced to cover the electrode surface, forming a protective layer. During the Joule heating modulation process, when the electrode temperature becomes too high, the heat is transferred to the surface pure water. The liquid water heats up, turns into steam, and evaporates, carrying away the excess heat from the modulation system, thus ensuring that the electrode surface structure is not damaged. High-resolution transmission electron microscopy of DEM-IrO_2@$Co(OH)_2$-NF (Figure 1d; Figure S9, Supporting Information) reveals the uniform embedding of IrO_2 clusters into $Co(OH)_2$, forming an interdigitated interface between IrO_2 and $Co(OH)_2$.[17] Figure 1e presents one set of doublets in the Ir 4f spectrum at 61.2 and 64.2 eV, attributed to Ir^{4+} of IrO_2.[18] Figure 1f illustrates that the main peak in the Co 2p region between 797.8 and 782.0 eV can be attributed to divalent Co^{2+}.[19] The primary peak in O1s corresponds to metal-oxygen bonds and surface hydroxyl oxygen (Figure 1g), consistent with the composition of DEM- IrO_2@$Co(OH)_2$-NF.[20] The above results show that electronic modulation process preserved the nanosheet structure of support and cluster size did not grow significantly.

2.2. Directed Electron Modulation of Active Center

After confirming that the supported catalyst was successfully constructed and that the catalyst structure was not destroyed during electronic modulation, we systematically investigated the changes in the electronic structure of the active center (IrO_2 cluster) during the modulation process. It has been previously mentioned that this study utilizes cyclic Joule heating strategy as a means for electronic modulation of the active center, specifically

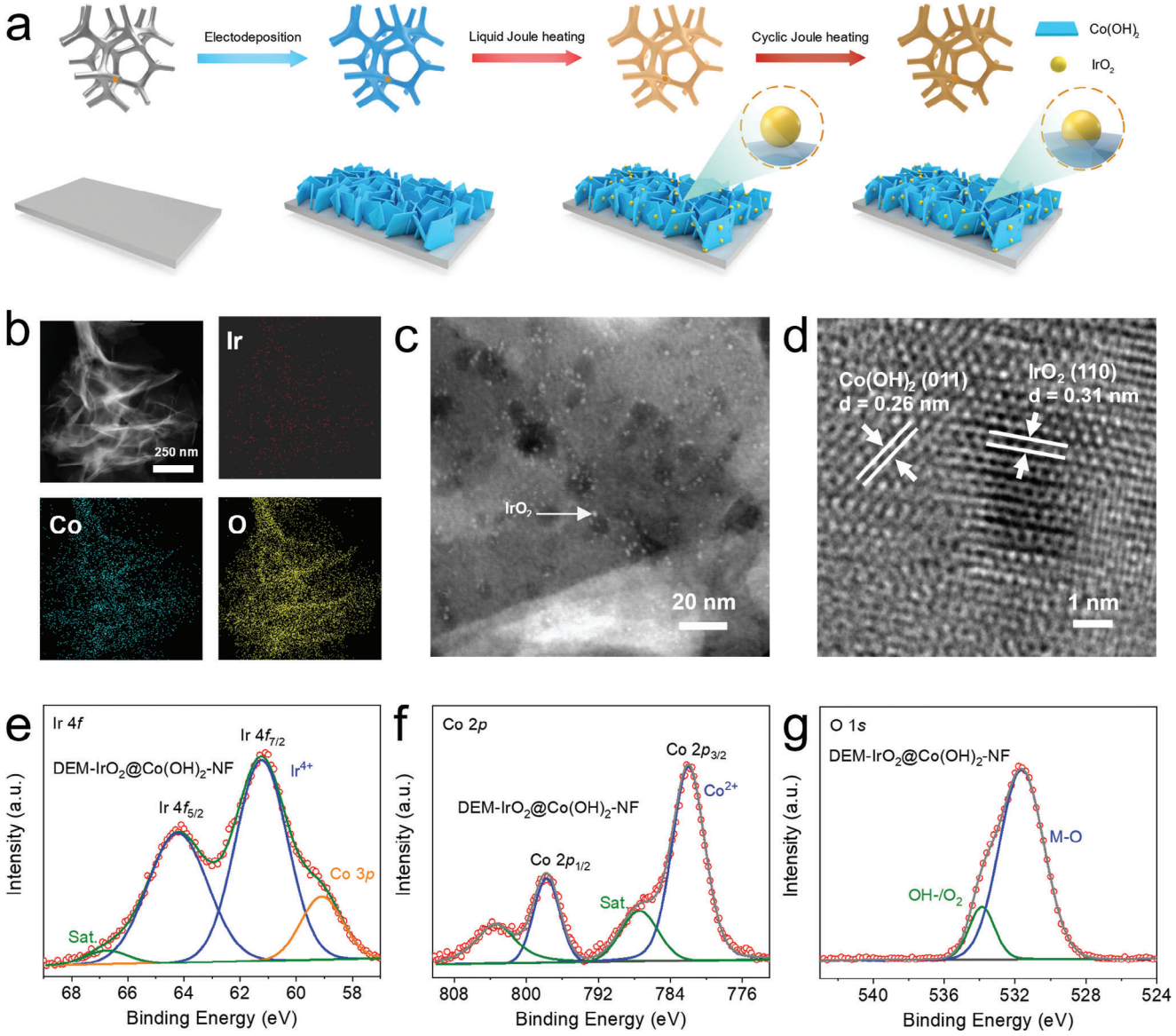

Figure 1. a) The schematic illustration of the synthesis of DEM-IrO2@Co(OH)2-NF electrode. b,c) HAADF-STEM image, Elemental mapping of Ir, Co, and O elements in DEM-IrO2@Co(OH)2-NF. d) HRTEM images of DEM-IrO2@Co(OH)2-NF. e) XPS spectra of Ir 4f in DEM-IrO2@Co(OH)2-NF. f) XPS spectra of Co 2p in DEM-IrO2@Co(OH)2-NF. g) XPS spectra of O 1s in DEM-IrO2@Co(OH)2-NF.

the rapid heating-cooling of Joule heating to achieve electron transfer between loading and support while ensuring the cluster size and support nanostructure. **Figure 2**a illustrates the temperature variation of the electrode during a single Joule heating cycle, with a heating duration of 4 s and a cooling duration of 2 s. The temperature is calibrated using a thermocouple. The electron transfer between support and loading during the modulation process was elucidated by analyzing the X-ray photoelectron spectroscopy (XPS) spectra of the samples subjected to different treatment cycles. The Ir 4f spectra (Figure 2b) show that the main peaks of Ir are all shifted toward lower binding energy as the number of treatment cycles increases. This implies that directed electron transfer between loading and support occurs during the modulation process, specifically, the transfer of electrons from $Co(OH)_2$ to Ir, resulting in a decrease in the valence state of Ir.[21] The Co 2p and O 1s spectra (Figure 2c,d) further confirmed the above judgment: after the initial loading of IrO_2 clusters, the main peaks of Co and O in $Co(OH)_2$ moved toward lower binding energies, which was attributed to the introduction of loading resulting in a change on the electronic structure of support. Subsequently, along with the electronic modulation process, the main peaks of Co and O were shifted toward higher binding energy, which indicated that electrons transferred from support to loading, resulting in the elevation of the valence states of Co and O in support. The above analysis results demonstrate that the cyclic Joule heating strategy successfully achieves directed electron modulation, in which electrons are transferred from support to loading and strong electron coupling is formed

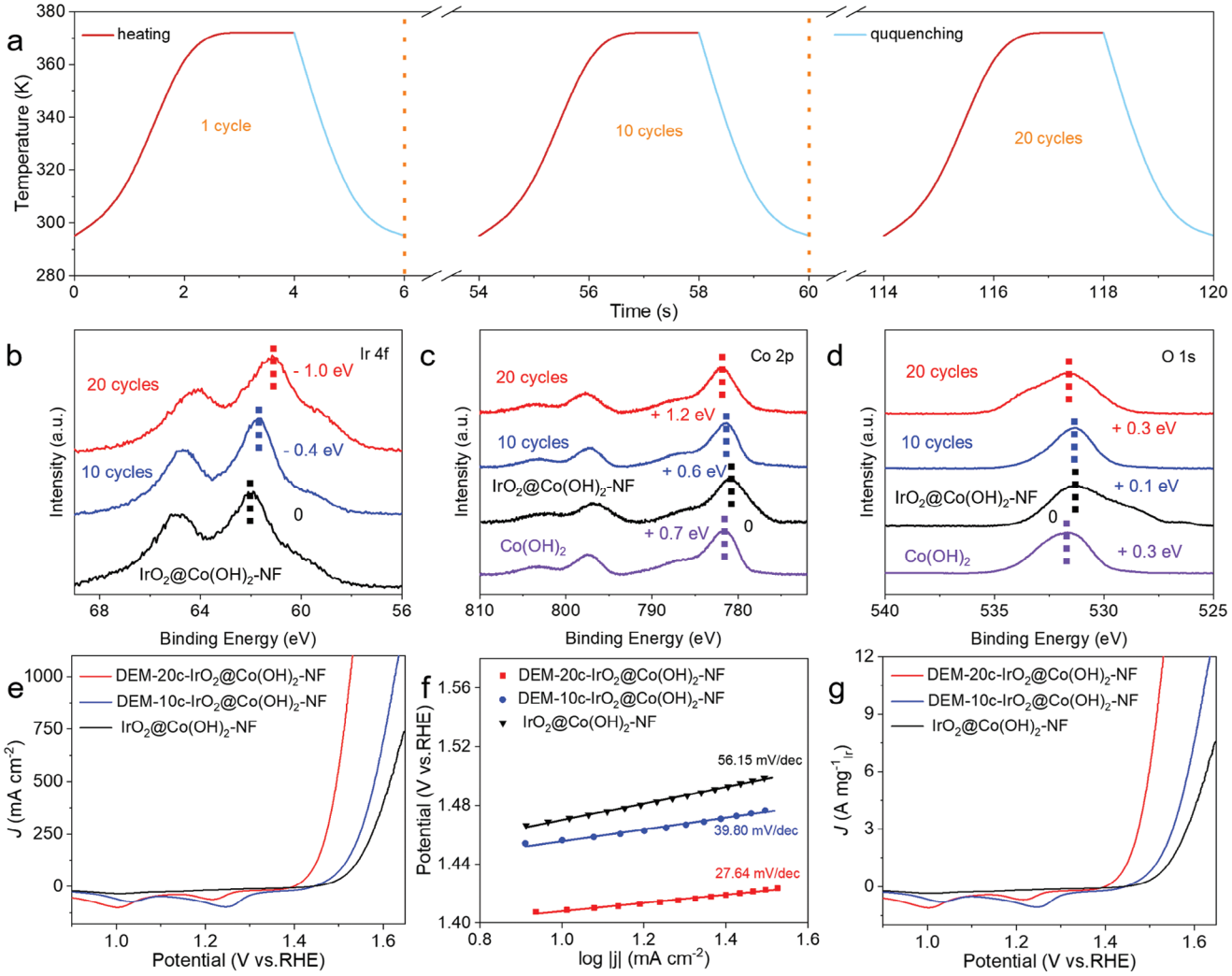

Figure 2. a) Temperature-time curve of heating and quenching process during cyclic Joule heating in pure water. b) XPS spectra of Ir 4*f* in initial IrO_2@$Co(OH)_2$-NF, 10 cycles, and 20 cycles. c) XPS spectra of Co 2*p* in initial IrO_2@$Co(OH)_2$-NF, 10 cycles, and 20 cycles. d) XPS spectra of O 1*s* in initial IrO_2@$Co(OH)_2$-NF, 10 cycles and 20 cycles. e) Polarization curves, (f) Tafel plots curves, and (g) The mass activity curves of IrO_2@$Co(OH)_2$-NF, DEM-10c- IrO_2@$Co(OH)_2$-NF and DEM-20c-IrO_2@$Co(OH)_2$-NF.

between the two. It is critical to the performance and stability of the catalyst during high current density operation.

The above results indicate that electrons transfer from the support to active center in the process of electron modulation using cyclic Joule heating. The electronic structure of the active center determines the adsorption capacity of reactants in an electrocatalytic reaction, so the catalytic performance of the electrode is bound to be transformed accordingly along with electron transfer in the modulation process. Figure 2e shows the performance of initial IrO_2@$Co(OH)_2$-NF and electrodes with different numbers of cyclic treatments. With the increase in the number of electrons transferred from support to loading during modulation, the deepening of electronic coupling between the two resulted in improved electrode performance. The initial IrO_2@$Co(OH)_2$-NF overpotential was 307 mV at 100 mA cm^{-2}, whereas the DEM-20c-IrO_2@$Co(OH)_2$-NF (DEM-IrO_2@$Co(OH)_2$-NF) overpotential after directed electron modulation was reduced by 91 mV, with only 216 mV overpotential. The Tafel slope analysis (Figure 2f) confirms that the directed electron modulation is accompanied by a decrease in the Tafel slope of electrodes, suggesting that the optimization of the electronic structure of the active center enhances the electrode reaction kinetics. Meanwhile, the mass-activity curves of electrodes (Figure 2g) showed that the mass-activity of electrodes was enhanced with the modulation process. Without significant changes in the cluster size, support nanostructure, and Ir loading, the mass activity enhancement indicates that intrinsic catalytic activity of the active center is enhanced during electron modulation.

2.3. Electrochemical Performance

After clarifying the electron transfer between support and loading during modulation, as well as the correlation between electron modulation and electrode performance, the directed

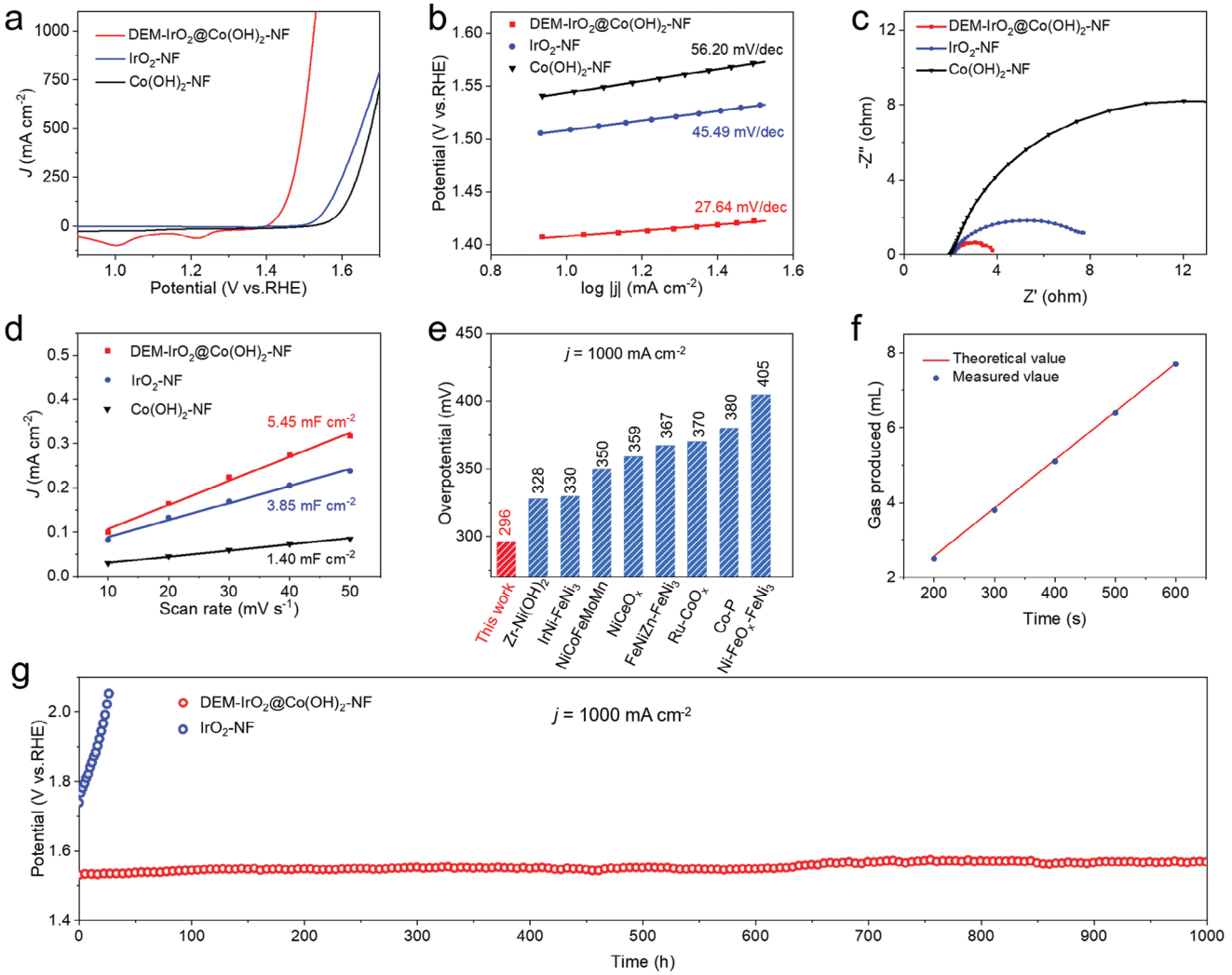

Figure 3. a) Polarization curves, and b) Tafel plots curves, and c) Nyquist plots, d) C_{dl} by plotting the current density variation of DEM-IrO_2@$Co(OH)_2$-NF, IrO_2-NF and $Co(OH)_2$-NF. e) Comparison of required overpotentials to reach the current densities of 1000 mA cm^{-2} between DEM-IrO_2@$Co(OH)_2$-NF and recently reported advanced OER catalysts. f) The evolution of theoretical oxygen volume and measured with time. g) Long-term durability test.

electron modulation electrode (DEM-IrO_2@$Co(OH)_2$-NF) was systematically characterized and compared with the commercially available IrO_2.

The polarization curves in **Figure 3a** illustrate that under the same current density, DEM-IrO_2@$Co(OH)_2$-NF exhibits the lowest reaction overpotential.[22a] At a current density of 100 mA cm^{-2}, the overpotentials for DEM-IrO_2@$Co(OH)_2$-NF, electrodeposited $Co(OH)_2$-NF, and commercial IrO_2-NF (with IrO_2 loading is 2 mg cm^{-2}) are 216, 376, and 332 mV, respectively. At a high current density of 1000 mA cm^{-2}, the overpotential required for DEM-IrO_2@$Co(OH)_2$-NF is 296 mV, significantly lower than that of commercial IrO_2-NF (506 mV). The exceptional catalytic activity of DEM-IrO_2@$Co(OH)_2$-NF can be attributed to the rapid charge transfer between IrO_2 and $Co(OH)_2$ due to strong electronic coupling and the optimized adsorption ability of reaction intermediates under their synergistic effects. This is manifested in the Tafel slope and EIS curves, where Figure 3b shows that DEM-IrO_2@$Co(OH)_2$-NF has the smallest Tafel slope, indicating its kinetic advantage. Figure 3c reveals that DEM-IrO_2@$Co(OH)_2$-NF has the smallest charge transfer resistance, implying faster charge transfer efficiency at the reaction interface. Further XPS results (Figure S10, Supporting Information) indicate that IrO_2-NF contains Ir(IV) and higher valence states of Ir, suggesting that the low-valence Ir in DEM-IrO_2@$Co(OH)_2$-NF is crucial for its excellent catalytic performance. By recording cyclic voltammograms, the electrochemical double-layer capacitance (C_{dl}) was used to assess the electrochemical active surface area (ECSA) of the electrode (Figure S11, Supporting Information). The results indicate that after loading iridium oxide clusters, the active area of DEM-IrO_2@$Co(OH)_2$-NF (5.45 mF cm^{-2}) has significantly increased compared to $Co(OH)_2$-NF (1.40 mF cm^{-2}), implying that the introduction of iridium oxide offers abundant active sites (Figure 3d). Furthermore, the OER activity of DEM-IrO_2@$Co(OH)_2$-NF surpasses that of most reported OER catalysts (Figure 3e; Table S4, Supporting Information).

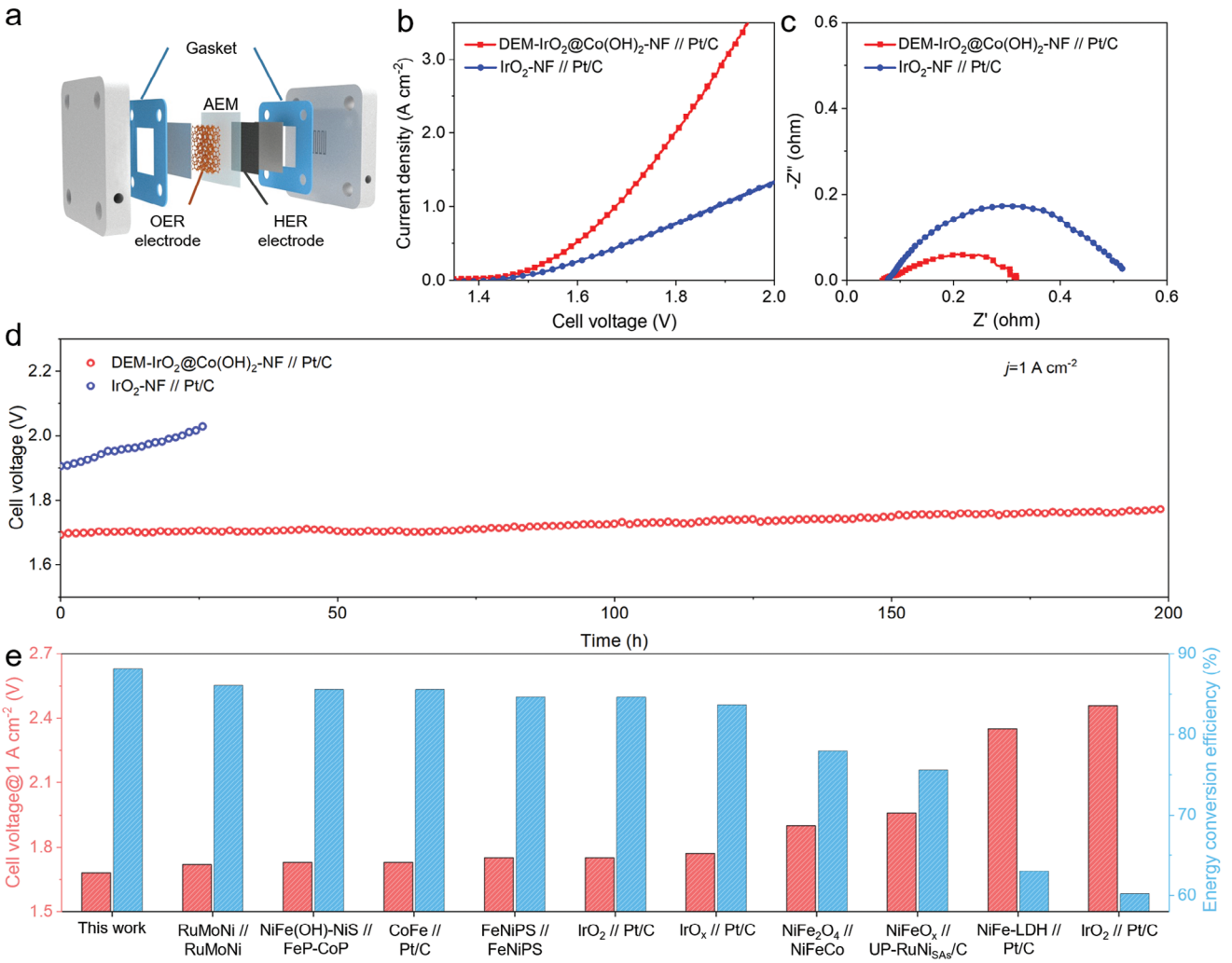

Figure 4. Overall water splitting using the AEM water electrolyzer. a) Structural schematic of the AEM electrolyzer. b) Polarization curves of the DEM-IrO_2@$Co(OH)_2$-NF||Pt/C compared to IrO_2-NF||Pt/C. c) Nyquist impedance plots of the AEM electrolyzers at 1.6 V. d) Durability cell voltage-time curve at 1 A cm^{-2} of DEM-IrO_2@$Co(OH)_2$-NF||Pt/C compared to IrO_2-NF||Pt/C. e) Cell voltage and energy conversion efficiency comparison of the cell using the DEM-IrO_2@$Co(OH)_2$-NF||Pt/C with other reported AEM water electrolyzer at 1 A cm^{-2}.

Considering that the complex OER process is often accompanied by other side reactions, it is necessary to verify the Faradaic efficiency of DEM-IrO_2@$Co(OH)_2$-NF electrode. The oxygen generated at DEM-IrO_2@$Co(OH)_2$-NF electrode side was collected at various time intervals, and it was observed to align well with the theoretical value, indicating the Faradaic efficiency close to 100% (Figure 3f).[22b] The OER durability was tested under a constant current of 1000 mA cm^{-2}, revealing that DEM-IrO_2@$Co(OH)_2$-NF displays significantly superior stability to iridium oxide over a testing period of 1000 h (Figure 3g; Figure S12, Supporting Information), with an overall decay rate of 0.038 mV h^{-1}. TEM images, XPS results, and ICP-OES results after the stability test showed that the iridium oxide clusters of DEM-IrO_2@$Co(OH)_2$-NF have not obviously detached (Figures S13–S15 and Table S2, Supporting Information), and the electronic structure of the catalyst did not change significantly. This exceptional performance is noteworthy in the context of supported noble metal catalyst systems, especially at an ultra-high current density of 1000 mA cm^{-2}. The electrochemical test results above indicate that DEM-IrO_2@$Co(OH)_2$-NF exhibits excellent activity and stability, with the potential for practical device applications. Furthermore, it confirms that creating strong electronic coupling between loading and support through the rapid heating-cooling strategy is essential for constructing a supported catalyst that operates efficiently and reliably under high current density.

2.4. Electrolyzer Device Construction and Performance

In order to further verify the operational status of the DEM-IrO_2@$Co(OH)_2$-NF electrode in practical water electrolysis devices, we assembled an anion exchange membrane (AEM) electrolyzer (**Figure 4a**; Figure S16, Supporting Information) with a DEM-IrO_2@$Co(OH)_2$-NF electrode as the anode and a Pt/C electrode as the cathode, and tested its performance using 1 M KOH

at 60 °C. Figure 4b demonstrates that the electrolyzer using DEM-IrO_2@$Co(OH)_2$-NF and Pt/C achieves a current density of 1 A cm^{-2} at 1.68 V, significantly outperforming the electrolyzer constructed by commercial IrO_2-NF||Pt/C (1 A cm^{-2} at 1.88 V). In the electrochemical impedance spectrum of cells (Figure 4c), the charge transfer resistance of cells using DEM-IrO_2@$Co(OH)_2$-NF is significantly lower than that of IrO_2-NF, which is apparently attributed to the high activity and rapid charge transfer kinetics of DEM-IrO_2@$Co(OH)_2$-NF catalytic electrode. Stability, as a crucial factor for device integrity, is a prerequisite for electrode transition from the laboratory to industrial production. A 200-h test was conducted at 1 A cm^{-2}, and the results indicate no significant performance deterioration of the electrolyzer using DEM-IrO_2@$Co(OH)_2$-NF as the anode (Figure 4d). The electrolyzer using commercial IrO_2-NF as the anode shows a clear performance degradation within 25 h. The excellent AEM electrolyzer performance and high energy conversion efficiency further confirm the promising practical application of electrodes with strong electronic coupling between loading and support (Figure 4e; Table S5, Supporting Information).

2.5. OER Mechanisms and Simulations

To investigate the effect of DEM-IrO_2@$Co(OH)_2$-NF on OER performance, density functional theory calculations were carried out. DEM-IrO_2@$Co(OH)_2$-NF is simulated by loading IrO_2 cluster on a two atomic layer (3 × 3) $Co(OH)_2$(001), and the atomic structures of IrO_2(110) and DEM-IrO_2@$Co(OH)_2$-NF are shown in **Figure 5a**. What should be noted is that the $Co(OH)_2$ slab in our model contains one bottom $Co(OH)_2$ layer and one top CoOOH layer, as the CoOOH layer will occur during OER process on $Co(OH)_2$ in the experiment and make stronger adsorption ability of IrO_2 cluster on it (Figure S18, Supporting Information).[23a] According to the calculated free energy changes of OER in Figure 5b, the intermediates (*OH, *O, and *OOH) adsorption ability of DEM-IrO_2@$Co(OH)_2$-NF are weaker than those of IrO_2(110), and the rate-determining step (RDS) of both of them is the second step of OER ($^*OH \rightarrow {}^*O + H^+ + e^-$).[23b] As the OER overpotential reduces from 0.66 eV on IrO_2(110) to 0.50 eV on IrO_2@$Co(OH)_2$-NF, indicating the higher OER activity of DEM-IrO_2@$Co(OH)_2$-NF. In addition, the calculated OER overpotential value on IrO_2(110) is close to previous work.[23c]

The electron gain and loss could unveil the stability and improved OER activity of DEM-IrO_2@$Co(OH)_2$-NF. Once the IrO_2 cluster adsorbs on $Co(OH)_2$-NF substrate, the electron transfer from $Co(OH)_2$ substrate to IrO_2 cluster is calculated to be 1.02 *e* (Figure 5c), which will produce a strong formation energy (−10.53 eV, Figure S18, Supporting Information) and a stable DEM-IrO_2@$Co(OH)_2$-NF. Further analysis shows that OER intermediate *O will gain more electron on DEM-IrO_2@$Co(OH)_2$-NF than that on IrO_2(110), and the gain electron of *O on former and later ones are 0.50 *e* and 0.39 *e*, respectively (Table S8, Supporting Information). The *OH could form by adsorbing one hydrogen atom on *O, which is the inverse process of the second OER step ($^*OH \rightarrow {}^*O + H^+ + e^-$). The more electron intermediate *O gain, the less electron gain of *O from the coming hydrogen atom further in the process of $^*O + H^+ + e^- \rightarrow {}^*OH$, which will lead to the weaker hydrogen adsorption ability on intermediate *O and larger free energy change of this process, or smaller free energy change of second OER step in other words. As more electron gain of *O on DEM-IrO_2@$Co(OH)_2$-NF than that on IrO_2(110), the free energy change of the second OER step, also the RDS, is smaller on the former one than that on the latter one. The smaller free change of RDS leads to smaller overpotential and improved OER activity on DEM-IrO_2@$Co(OH)_2$-NF.

In situ electrochemical Raman spectrum (Figure S19, Supporting Information) was further employed to decipher the key role of directed electron modulation on OER performance of the active center. The Raman peaks attributed to $Co(OH)_2$ (the peaks at 457 cm^{-1} and 517 cm^{-1})[23a] and IrO_2 (the peak at 564 cm^{-1})[24] in DEM-IrO_2@$Co(OH)_2$-NF at OCP can be observed in Figure 5d. As voltage is applied, the conversion of Co-OH to Co-OOH occurs under the action of oxidation potential.[23a] At an applied voltage of 1.48 V, Ir-O in DEM-IrO_2@$Co(OH)_2$-NF is converted to Ir-OH (the peak at 685 cm^{-1}),[24] which corresponds to RDS of DEM-IrO_2@$Co(OH)_2$-NF in DFT results. Subsequently, the peak of Ir—OH remained stable with increasing voltage, indicating that the OER process of DEM-IrO_2@$Co(OH)_2$-NF was limited by the reaction energy barrier of RDS and the RDS reactant accumulated. As shown with the in situ Raman spectrum of IrO_2-NF (Figure 5e), Ir-O (the peak at 553 cm^{-1}) in IrO_2-NF is converted to Ir-OOH (The broad peaks at 502 cm^{-1} and 841 cm^{-1})[24] only at an applied voltage of 1.53 V. Compared with DEM-IrO_2@$Co(OH)_2$-NF, the structural phase transition of IrO_2-NF occurs at a higher voltage, which implies that the reaction kinetics of IrO_2-NF is slower and a higher overpotential is required for OER to occur. The results of DFT and in situ Raman spectrum indicated that the directed electron modulation optimizes the adsorption ability of reaction intermediates in the active center and the reaction kinetics are enhanced.

3. Conclusion

In this work, we designed the cyclic Joule heating strategy to achieve directed electronic structure modulation of the active center. The strategy utilizes the rapid heating-cooling properties of Joule heating to achieve strong electronic coupling between cluster and support while maintaining the nanostructure and cluster size of the initial catalyst. Based on the strong electronic coupling between IrO_2 and $Co(OH)_2$ as well as abundant active sites of2D structures, the DEM-IrO_2@$Co(OH)_2$-NF exhibited ultrahigh OER catalytic performance, reaching a current density of 1000 mA cm^{-2} at an overpotential of 296 mV in alkaline electrolyte, and operated stably for 1000 h. This work provides an effective strategy for the construction and optimization of supported catalysts suitable for industrial high current density.

4. Experimental Section

Synthesis of the Co(OH)$_2$-NF: Cobalt nitrate hexahydrate ($Co(NO_3)_2$•$6H_2O$, AR, 99%, Macklin), Sodium nitrate ($NaNO_3$, AR, 99.0%, Aladdin), Nickel foam (Lizhiyuan Co. Ltd.), hydrochloric acid (HCl, 37%, Sinopharm Chemical Reagent Co., Ltd.) and deionized water were used as received without any further purification. The nickel foam (1 cm × 4 cm × 1 mm) was first sonicated in a 3 mol L^{-1} hydrochloric acid solution for 10 min, and then treated with ethanol and deionized water in an ultrasonic bath for 10 min to remove impurities and oil from

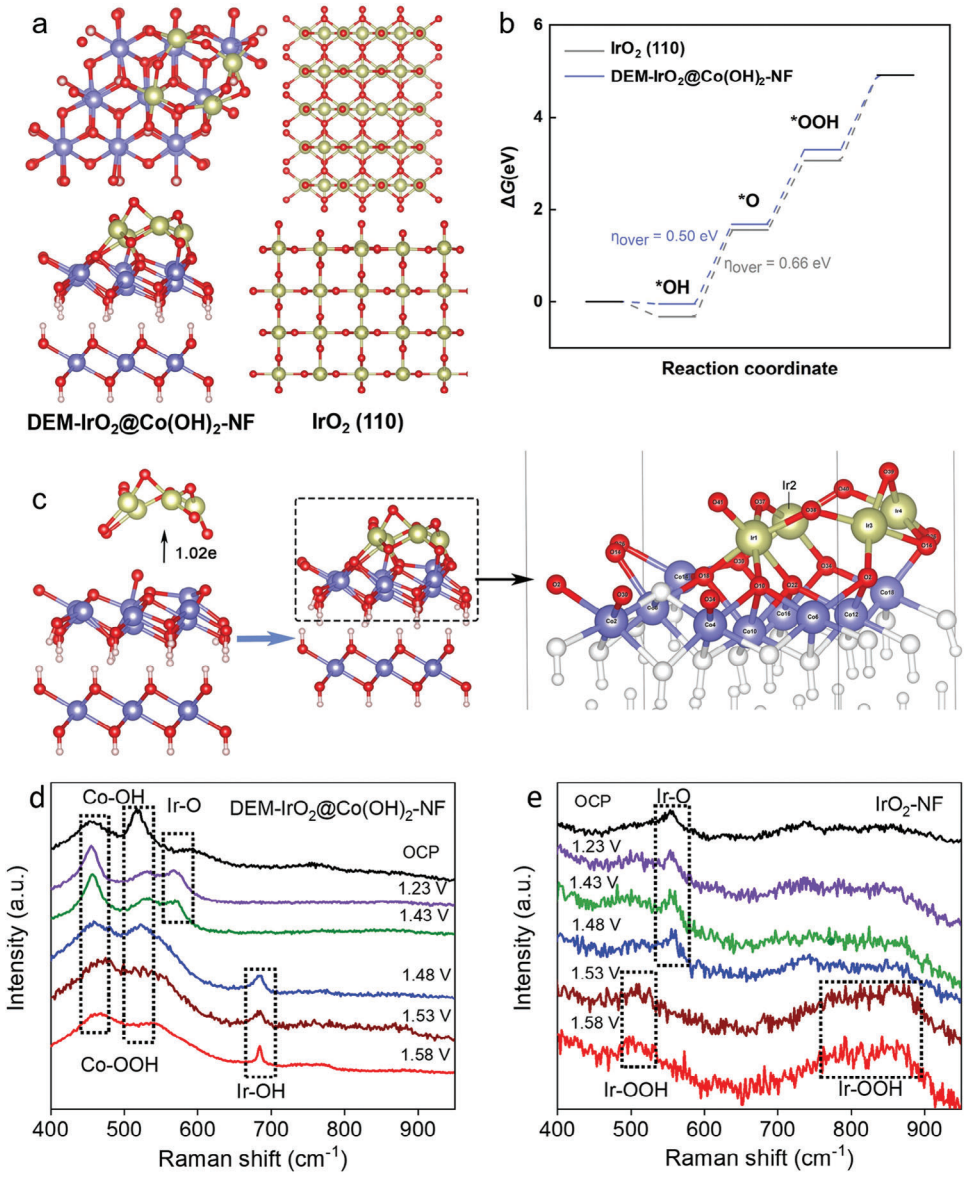

Figure 5. Reaction energy diagrams of alkaline OER over the DEM-IrO_2@$Co(OH)_2$-NF site. a) The top and side views of atomic structures of DEM-IrO_2@$Co(OH)_2$-NF and IrO_2(110). b) The free energy diagram of OER on DEM-IrO_2@$Co(OH)_2$-NF and IrO_2(110). All data are in Table S6 (Supporting Information). c) Charge transfer on *O-adsorbed DEM-IrO_2@$Co(OH)_2$-NF. All data are in Table S7 (Supporting Information). In situ Raman spectra of DEM-IrO_2@$Co(OH)_2$-NF d) and IrO_2-NF e) in 1 M KOH under different applied potentials.

the surface. The cathodic deposition of $Co(OH)_2$ was carried out on a CHI660E electrochemical workstation using a two-electrode system in 0.01 M $Co(NO_3)_2$ and 0.1 M $NaNO_3$, with the working electrode being nickel foam and the counter electrode being a carbon rod. The deposition current density was 10 mA cm^{-2} and the time was 900 s.

Synthesis of the IrO_2@$Co(OH)_2$-NF and DEM-IrO_2@$Co(OH)_2$-NF: Iridium chloride (IV) hydrate ($IrCl_4{\cdot}xH_2O$, Ir 48.0–55.0%, Macklin) and deionized water were used as received without any further purification. The $Co(OH)_2$-NF was dipped into the prepared iridium chloride (IV) aqueous solution (0.5 mM) until the surface of $Co(OH)_2$-NF was completely covered with liquid. Then both ends of the $Co(OH)_2$-NF connected to a DC power supply through copper clamps, and IrO_2@$Co(OH)_2$-NF was prepared by power output of 200 W from the power supply for 20 s. The loading of Ir in IrO_2@$Co(OH)_2$-NF was 0.098 mg cm^{-2}.

The IrO_2@$Co(OH)_2$-NF was completely covered with deionized water and then connected to a DC power supply and output 150 W for 4 s. This was one cycle of the electron modulation process using cyclic Joule heating. Ten cycles of the process yielded DEM-10c-IrO_2@$Co(OH)_2$-NF. Twenty cycles of the process yielded DEM-20c-IrO_2@$Co(OH)_2$-NF, which was also DEM-IrO_2@$Co(OH)_2$-NF. The loading of Ir in DEM-IrO_2@$Co(OH)_2$-NF was 0.091 mg cm^{-2}.

Iridium oxide (IrO_2, 99.95%, Sinero). The IrO_2-NF was prepared on nickel foam using ultrasonic spraying method (the loading of IrO_2 as 2 mg cm^{-1}). The IrO_2 loading was chosen to follow the common commercial water electrolysis equipment with an iridium loading of 1–2 mg cm^{-2}.

Material Characterizations: X-ray diffraction analysis was performed using a D/max 2500 V diffractometer in reflection mode at 40 kV and 150 mA, and at a scanning speed of 8 °C min-1. Laser ICP analysis of

Ir was performed using an inductively coupled plasma-optical emission spectrometer (Vista-MPX). Scanning electron microscopy (SEM) images were recorded with a scanning electron microscope (LEO-1530, Zeiss, Germany) at an acceleration voltage of 20 kV. HAADF STEM images, TEM images, and EDX analysis were carried out on a 2100F transmission electron microscope operated at 200 kV and an aberration correction-transmission electron microscope (JEM-ARM200F) operated at an accelerating voltage of 200 kV. XPS measurements were obtained using an X-ray photoelectron spectrometer (Escalab, 250 Xi, Thermo Fisher Scientific, MA, USA) equipped with an Al Kα radiation source (1487.6 eV) and a hemispherical analyzer with a pass energy of 30.0 eV and an energy step size of 0.05 eV. The binding energy of the C 1s peak at 284.8 eV was considered as an internal reference. The raw curves were fitted with Shirley backgrounds and Gaussian-Lorentzian functions using XPSPEAK41 software.

Electrochemical Measurement: Electrocatalytic activity tests were performed in a three-electrode system using an electrochemical workstation (EnergyLab XM + External Booster, Solartron Analytical). The OER performance of working electrodes was measured at 25 °C in a three-electrode system, in which a graphite rod and a Hg/HgO reference electrode were used as the counter electrode and the reference electrode, respectively. For three-electrode measurements, the geometric area of the working electrode was 0.4*0.5 cm^{-2} and the electrolyte was 1 M KOH solution. All potentials applied in 1.0 M KOH were calibrated to RHE using the following equation: $E_{RHE} = E_{Hg/HgO} + 0.098 + 0.059 \times pH$. Polarization curves were measured by linear sweep voltammetry (LSV) at a scan rate of 5 mV s^{-1} and compensated using 95% iR compensation. Cyclic voltammograms (CV) were recorded at increasing scan rates (10-50 mV s^{-1}) within a non-Faradaic potential window to obtain electrochemical surface area (ECSA). Electrochemical impedance spectroscopy (EIS) was performed in the frequency range of 10^5-0.01 Hz with an amplitude of 10 mV. The long-term stability performance was operated at the current density of 1000 mA cm^{-2}.

Testing of the AEM Electrolyzer: The AEM electrolyzer was evaluated using a single-cell test. The cathode was Pt/C prepared on carbon paper by the ultrasonic spraying method (the loading of Pt was 1.0 mg cm^{-1}). The cell temperature was maintained at 60 °C under atmospheric pressure, and the active area was 1 cm^{-2}. Preheated reactant (1 M KOH) was supplied to both sides at a flow rate of 10 mL min^{-1}. The Dioxide Materials Sustainion X37-50 grade RT was used as a diaphragm. The alkaline electrolyzer performance was evaluated via the voltage sweep method from 1.2 to 2.0 V at a scan rate of 10 mV s^{-1} using an electrochemical workstation (EnergyLab XM + External Booster, Solartron Analytical). Electrochemical impedance spectroscopy (EIS) was performed at a constant voltage of 1.6 V with an amplitude of 10 mV to analyze the resistance of the alkaline electrolyzer. The durability of the AEM electrolyzer was evaluated using chronoamperometry at a current density of 1000 mA cm^{-2}. The energy conversion efficiency was calculated according to the following equations: 1) $\eta = E_0/V$; 2) $E_0 = -\Delta H/nF$, where η is the energy conversion efficiency and E_0 is the theoretical voltage of water splitting ($H_2O \rightarrow H_2 + 1/2O_2$). n is the number of electrons, F is the Faradaic constant (96 485 C mol^{-1}), V is the measured voltage and ΔH is the change of enthalpy (-285.8 kJ mol^{-1}) during water electrolysis.

Supporting Information

Supporting Information is available from the Wiley Online Library or from the author.

Acknowledgements

X.H. and J.T. contributed equally to this work. This work was supported by the National Natural Science Foundation of China (NSFC) No. 52472087, Basic Science Center Program of NSFC Grant No. 52388201, NSFC Grant No. 52325312, State Key Laboratory of New Ceramic and Fine Processing Tsinghua University No. KFZD202305, Beijing Municipal Science & Technology Commission, Administrative Commission of Zhongguancun Science Park No. Z231100006023020, NSFC Grant No. 52203043, Fundamental Research Funds for the Central Universities (2023ZCJH03, 2021XD-A041), Fund of State Key Laboratory of Information Photonics and Optical Communications (Beijing University of Posts and Telecommunications, P.R. China), Teaching Reform Projects at BUPT (2022CXCY-B03).

Conflict of Interest

The authors declare no conflict of interest.

Data Availability Statement

The data that support the findings of this study are available from the corresponding author upon reasonable request.

Keywords

directed electron modulation, high-current-density, iridium-based catalysts, oxygen evolution reaction

Received: September 3, 2024
Revised: October 29, 2024
Published online:

[1] D. Guan, H. Xu, Q. Zhang, Y.-C. Huang, C. Shi, Y.-C. Chang, X. Xu, J. Tang, Y. Gu, C.-W. Pao, S.-C. Haw, J.-M. Chen, Z. Hu, M. Ni, Z. Shao, *Adv. Mater.* **2023**, *35*, 2305074.
[2] Y. L. Xu, C. Wang, Y. H. Huang, J. Fu, *Nano Energy* **2021**, *80*, 105545.
[3] N. Govindarajan, G. Kastlunger, H. H. Heenen, K. Chan, *Chem. Sci.* **2021**, *13*, 14.
[4] V. V. Welborn, L. R. Pestana, T. Head-Gordon, *Nat. Catal.* **2018**, *1*, 649.
[5] C. Z. Wan, Z. S. Zhang, J. C. Dong, M. J. Xu, H. T. Pu, D. Baumann, Z. Y. Lin, S. B. Wang, J. Huang, A. H. Shah, X. Q. Pan, T. D. Hu, A. N. Alexandrova, Y. Huang, X. F. Duan, *Nat. Mater.* **2023**, *22*, 1022.
[6] X. Y. Yang, L. H. Chen, Y. Li, J. C. Rooke, C. Sanchez, B. L. Su, *Chem. Soc. Rev.* **2017**, *46*, 481.
[7] Y. Li, Z.-Y. Fu, B.-L. Su, *Adv. Funct. Mater.* **2012**, *22*, 4634.
[8] A. Li, S. Kong, K. Adachi, H. Ooka, K. Fushimi, Q. Jiang, H. Ofuchi, S. Hamamoto, M. Oura, K. Higashi, T. Kaneko, T. Uruga, N. Kawamura, D. Hashizume, R. Nakamura, *Science* **2024**, *384*, 666.
[9] P. C. Wang, B. G. Wang, *ACS Appl. Mater. Interfaces* **2021**, *13*, 59593.
[10] P. Babar, A. Lokhande, H. H. Shin, B. Pawar, M. G. Gang, S. Pawar, J. H. Kim, *Small* **2018**, *14*, 1702568.
[11] Y. T. Luo, Z. Y. Zhang, M. Chhowalla, B. L. Liu, *Adv. Mater.* **2022**, *34*, 2108133.
[12] Y. K. Zhang, Y. X. Lin, T. Duan, L. Song, *Mater. Today* **2021**, *48*, 115.
[13] J. Xu, Z. Lian, B. Wei, Y. Li, O. Bondarchuk, N. Zhang, Z. Yu, A. Araujo, I. Amorim, Z. Wang, B. Li, L. Liu, *ACS Catal.* **2020**, *10*, 3571.
[14] S. Mitchell, J. Pérez-Ramírez, *Nat. Rev. Mater.* **2021**, *6*, 969.
[15] X. Hu, X. Tian, Y. Lin, Z. Wang, *RSC Adv.* **2019**, *9*, 31563.
[16] J. Zhang, J. Dang, X. Zhu, J. Ma, M. Ouyang, F. Yang, *Appl. Catal. B-Environ.* **2023**, *325*, 122296.
[17] S. Ge, R. Xie, B. Huang, Z. Zhang, H. Liu, X. Kang, S. Hu, S. Li, Y. Luo, Q. Yu, J. Wang, G. Chai, L. Guan, H. Cheng, B. Liu, *Energy Environ. Sci.* **2023**, *16*, 3734.
[18] V. Pfeifer, T. E. Jones, J. J. V. Vélez, C. Massué, R. Arrigo, D. Teschner, F. Girgsdies, M. Scherzer, M. T. Greiner, J. Allan, M. Hashagen, G. Weinberg, S. Piccinin, M. Hävecker, A. Knop-Gericke, R. Schlögl, *Surf. Interface Anal.* **2016**, *48*, 261.
[19] H. R. Jiang, S. Q. Zhao, X. L. Ma, S. J. Liu, Q. Shen, *J. Power Sources* **2019**, *426*, 23.

[20] L. Zhang, L. Wang, Y. Wen, F. Ni, B. Zhang, H. Peng, *Adv. Mater.* **2020**, *32*, 2002297.
[21] W. Zhu, X. Song, F. Liao, H. Huang, Q. Shao, K. Feng, Y. Zhou, M. Ma, J. Wu, H. Yang, H. Yang, M. Wang, J. Shi, J. Zhong, T. Cheng, M. Shao, Y. Liu, Z. Kang, *Nat. Commun.* **2023**, *14*, 5365.
[22] a) D. Guan, K. Zhang, Z. Hu, X. Wu, J. L. Chen, C. W. Pao, Y. Guo, W. Zhou, Z. Shao, *Adv. Mater.* **2021**, *33*, 2103392. b) L. Wan, M. B. Pang, J. F. Le, Z. Xu, H. Y. Zhou, Q. Xu, B. G. Wang, *Nat. Commun.* **2022**, *13*, 7956.
[23] a) C. Jing, T. Yuan, L. Li, J. Li, Z. Qian, J. Zhou, Y. Wang, S. Xi, N. Zhang, H.-J. Lin, C.-T. Chen, Z. Hu, D.-W. Li, L. Zhang, J.-Q. Wang, *ACS Catal.* **2022**, *12*, 10276; b) F. Abdelghafar, X. Xu, D. Guan, Z. Lin, Z. Hu, M. Ni, H. Huang, T. Bhatelia, S. P. Jiang, Z. Shao, *ACS Mater. Lett.* **2024**, *6*, 2985. c) Q. He, S. C. Qiao, Q. Zhou, Y. Z. Zhou, H. W. Shou, P. J. Zhang, W. J. Xu, D. B. Liu, S. M. Chen, X. J. Wu, L. Song, *Nano Lett.* **2022**, *22*, 3832.
[24] S. Y. Chen, S. S. Zhang, L. Guo, L. Pan, C. X. Shi, X. W. Zhang, Z. F. Huang, G. D. Yang, J. J. Zou, *Nat. Commun.* **2023**, *14*, 4127.